

MicroPush: A Simulator and Benchmark for Contact-Rich Cell Pushing and Assembly with a Magnetic Rolling Microrobot

Yanda Yang and Sambaeta Das

Abstract—Magnetic rolling microrobots enable gentle manipulation in confined microfluidic environments, yet autonomy for contact-rich behaviors such as cell pushing and multi-target assembly remains difficult to develop and evaluate reproducibly. We present *MicroPush*, an open-source simulator and benchmark suite for magnetic rolling microrobots in cluttered 2D scenes. *MicroPush* combines an overdamped interaction model with contact-aware stick-slip effects, lightweight near-field damping, optional Poiseuille background flow, and a calibrated mapping from actuation frequency to free-space rolling speed. On top of the simulator core, we provide a modular planning-control stack with a two-phase strategy for contact establishment and goal-directed pushing, together with a deterministic benchmark protocol with fixed tasks, staged execution, and unified CSV logging for single-object transport and hexagonal assembly. We report success, time, and tracking metrics, and an actuation-variation measure $E_{\Delta\omega}$. Results show that controller stability dominates performance under flow disturbances, while planner choice can influence command smoothness over long-horizon sequences via waypoint progression. *MicroPush* enables reproducible comparison and ablation of planning, control, and learning methods for microscale contact-rich micromanipulation.

NOTE TO PRACTITIONERS

Contact-rich micromanipulation with magnetic rolling microrobots is difficult to reproduce across laboratories because performance depends on calibration, disturbances (e.g., background flow), and intermittent contact dynamics. MicroPush helps practitioners prototype and benchmark planning and control pipelines before slow and delicate wet-lab trials. It offers an interactive GUI for rapid debugging and qualitative diagnosis, and a headless runner that executes deterministic, seed-controlled test suites for transport and multi-target assembly with standardized CSV logs and videos. MicroPush provides clean interfaces to swap global planners, task-level planners, and controllers without changing the simulator core, and also supports Gym-style evaluation of learned policies under the same protocols. While it uses a lightweight 2D overdamped model rather than high-fidelity fluid-structure simulation, it is designed for apples-to-apples comparisons, controlled ablations, and reproducible reporting of algorithmic improvements under clutter and flow.

Index Terms—Microrobotics, magnetic rolling microrobots, contact-rich manipulation, simulation and benchmarking, planning and control, multi-target assembly, reproducibility.

Y. Yang and S. Das are with the Department of Mechanical Engineering, University of Delaware, Newark, DE 19716, USA (e-mail: roboty@udel.edu; samdas@udel.edu).

I. INTRODUCTION

Microscale robotic manipulation is increasingly important for biomedical automation and tissue engineering [1]–[3], where precise and gentle interaction with fragile biological targets is required in confined microfluidic environments. Magnetically actuated rolling microrobots are particularly attractive in this setting: they can be driven wirelessly without onboard power, operate near surfaces, and exert forces compatible with living cells while enabling behaviors such as transport, sorting, and pattern formation [4]–[8]. Among these behaviors, contact-rich micromanipulation is a practical pathway to programmable cell placement and small-scale assembly [9]–[11]. However, developing robust autonomy for contact-rich pushing and multi-target assembly remains difficult, and, critically, existing results are often hard to reproduce and compare across methods and laboratories.

Two factors make this problem uniquely challenging. First, the microscale interaction regime couples several dominant effects that strongly influence outcomes [12], [13]: overdamped, viscous-dominated motion at low Reynolds number; near-wall hydrodynamics; frictional stick-slip; intermittent contact loss; and environmental disturbances such as background flow. Small variations in contact state or near-field resistance can lead to qualitatively different trajectories, making failure modes frequent and hard to diagnose. Second, physical experimentation is slow and delicate [14]–[16]: calibration and hardware conditions vary across platforms, repeated trials at scale are difficult, and extensive ablations or learning-based training can risk damaging samples. These realities create a practical bottleneck: even when new planning, control, or learning ideas are available, the lack of a unified, reproducible toolchain makes it hard to test hypotheses quickly, run controlled “what-if” studies, and report apples-to-apples comparisons under aligned tasks, metrics, and protocols.

In macrorobotics, open simulators [17]–[19] and standardized benchmarks [20]–[23] have accelerated progress by aligning tasks, evaluation metrics, scenario generation, and baseline implementations, enabling reproducible comparisons and controlled ablations. In micromanipulation, several platforms have been proposed for specific actuation modalities and interaction settings [24], [25], including recent simulation environments for optical-tweezer-driven microrobotics that integrate RL modules and interactive interfaces for cell manipulation tasks [16]. However, comparable tooling remains limited for magnetically driven, surface-rolling microrobots that

perform contact-rich cell pushing and multi-target assembly under clutter and flow. Existing micromanipulation platforms often emphasize system demonstrations or modality-specific autonomy and typically do not provide a unified benchmark suite that combines (i) deterministic, seed-controlled scenario generation, (ii) standardized success criteria and metrics, and (iii) consistent logging and evaluation scripts for repeatable, fair comparisons across methods [24]–[26]. Meanwhile, general contact-rich manipulation benchmarks typically focus on macroscopic dynamics [27], [28] and do not capture characteristic microscale phenomena such as overdamped motion, near-field resistance, and stick–slip interactions. As a result, researchers lack an open foundation that captures the key interaction effects needed for rolling microrobot pushing, exposes clean interfaces for swapping planners, controllers, and learning policies, and standardizes tasks, metrics, protocols, and baselines for controlled ablations and apples-to-apples evaluation.

We address this gap with *MicroPush*, an open-source simulator and benchmark suite for contact-rich cell pushing and assembly with magnetically actuated rolling microrobots in cluttered 2D scenes. *MicroPush* is designed as an end-to-end engineering toolchain rather than a standalone physics model, targeting dominant-effect fidelity for algorithm development and reproducible evaluation: it provides an interactive environment and a headless benchmark runner; deterministic, seed-controlled scenario generation; unified per-episode logging; and standardized metrics and evaluation scripts. The simulator adopts a lightweight yet physics-grounded 2D overdamped model that captures dominant effects for rolling microrobot pushing, including contact-aware stick–slip interactions, near-field hydrodynamic damping, and optional Poiseuille background flow, together with a calibrated mapping from actuation frequency to free-space rolling speed. On top of the simulator core, *MicroPush* exposes a modular planning–control stack and an RL-ready interface and includes reference baselines, including a practical two-phase manipulation strategy that first establishes stable contact and then executes goal-directed pushing. This design enables rapid iteration on autonomy modules and controlled, reproducible comparisons across planning, control, and learning methods before transitioning to hardware.

Our contributions can be summarized as follows:

- 1) **Physics-grounded, efficient simulator core:** a computationally lightweight simulator for magnetic rolling microrobot–cell interactions that captures overdamped motion, stick–slip contact, near-field damping, and optional background flow, with calibrated actuation and deterministic seeding.
- 2) **Modular autonomy interfaces and reference baselines:** clean, swappable interfaces for planners, controllers, and learning-based policies via an RL-compatible wrapper, together with reference baseline implementations to support stable contact-rich manipulation and systematic method replacement.
- 3) **Standardized, reproducible benchmark suite:** deterministic task protocols, seed-controlled scene generation, unified logging, and standardized metrics for canonical tasks including single-object transport with

or without flow and multi-target hexagonal assembly, enabling apples-to-apples evaluation and controlled ablations.

The remainder of the paper presents the system architecture and simulator model, describes the planning and control modules and interfaces, and then details the benchmark tasks, metrics, and experimental results.

II. MICROPUSH: ARCHITECTURE AND CORE MODULES

MicroPush is an open-source simulation and benchmarking platform for contact-rich micromanipulation with magnetically actuated rolling microrobots, with a focus on indirect cell pushing and multi-target assembly in cluttered 2D workspaces. As summarized in Fig. 1, *MicroPush* follows a modular closed-loop architecture that cleanly separates (i) an interactive user front end, (ii) a physics-based simulator core, (iii) interchangeable planning and control modules, and (iv) standardized benchmarking and logging utilities. This separation enables researchers to (a) iterate quickly in an interactive environment, (b) run large-scale headless evaluations under identical protocols, and (c) swap planners/controllers without modifying the simulator core.

A. System overview

MicroPush supports two complementary usage modes. (1) Interactive prototyping: a GUI provides real-time visualization, a control panel, and runtime readouts (e.g., actuation frequency, heading, and robot/cell velocities) to facilitate rapid debugging and qualitative diagnosis (see Movies S1–S2 for representative interactive operation and direction-control pushing). (2) Headless benchmarking: scripted evaluation runs the same simulator and tasks without rendering, logs per-episode trajectories and metrics in a unified CSV schema, and optionally records synchronized videos for inspection.

At the core, the simulator exposes a minimal API (reset, step, and observation) to support both human-in-the-loop operation and automated evaluation. The simulator models low-Reynolds-number planar motion using an overdamped formulation, incorporates contact-aware interactions for pushing, optional Poiseuille background flow, and a calibrated mapping from actuation inputs (frequency and heading) to free-space rolling speed. It returns structured observations consumed by downstream planners/controllers and by learning-based interfaces.

On top of the simulator, *MicroPush* provides a modular planning and control stack. The planning layer includes obstacle-aware global planners (Analytic Geometry Planner (AGP) and weighted A*) and a task-level planner for hexagonal assembly that outputs target assignment and intermediate subgoals. The control layer implements baseline controllers (MPC and PID) under a shared two-stage manipulation strategy: the system first establishes stable contact and then executes goal-directed pushing. In addition, *MicroPush* wraps the same simulator and task definitions into a Gym-style interface, enabling reinforcement learning methods to interact with identical dynamics, disturbances, and evaluation protocols.

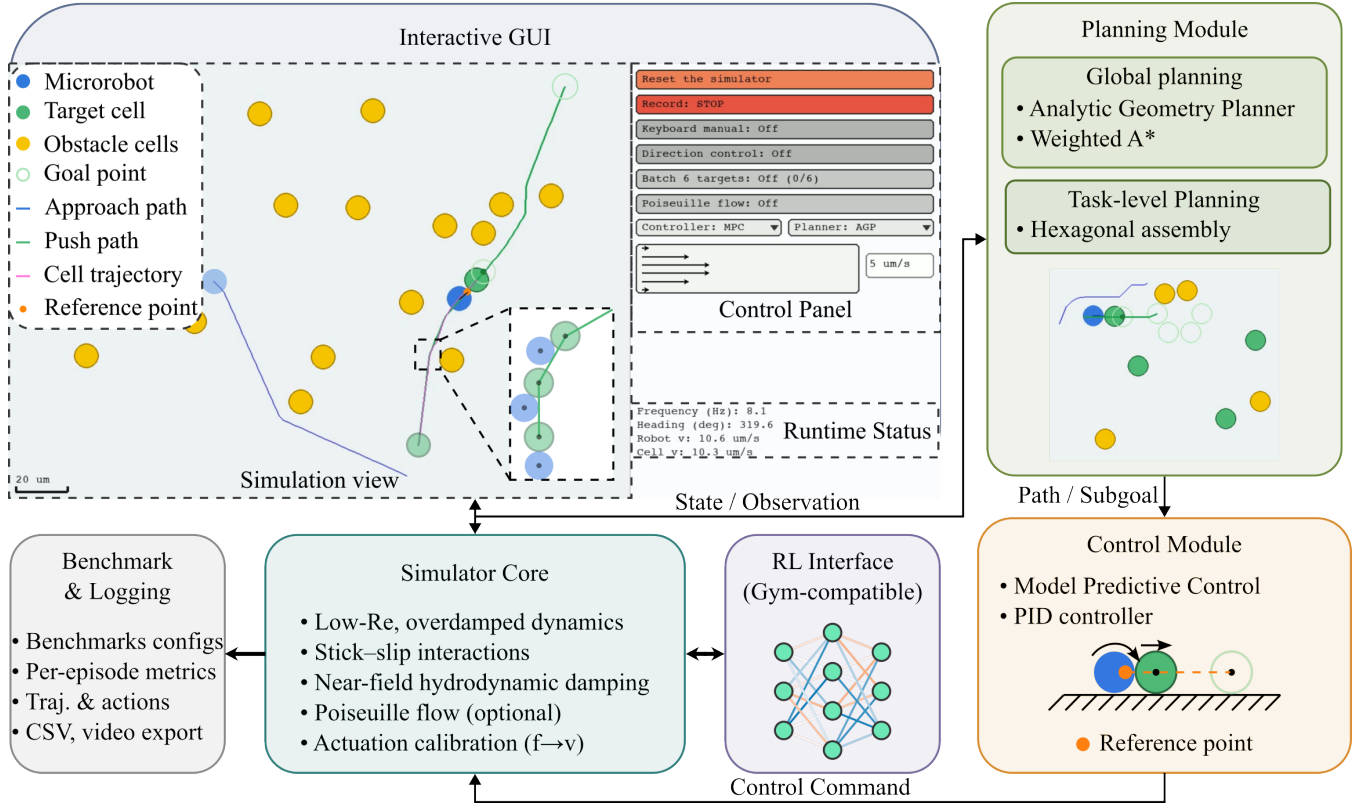


Fig. 1. **System overview of MicroPush.** MicroPush consists of an interactive GUI, a physics-based simulator core, interchangeable planning and control modules, a Gym-compatible RL interface, and standardized benchmarking and logging utilities. The modular design supports both interactive prototyping and headless batch evaluation under consistent tasks, metrics, and logging. See Movie S3 for a representative flow-off transport execution.

B. Extensibility and interfaces

MicroPush is designed to be extensible at three levels: simulation, algorithm modules, and evaluation. At the simulation level, the engine exposes a minimal step-based API shared by the interactive GUI and the headless runner. At each step, the user supplies an actuation command (ω, θ) , the engine advances the world by one simulation step, and an observation dictionary is returned. Observations include robot state, per-cell states, and geometry, with quantities available in both simulator coordinates and physical units. This interface allows new controllers, planners, and learning agents to be integrated without modifying the simulator core.

At the algorithm level, planners and controllers follow a common input and output contract. Global planners consume the current world state and output a resampled polyline in pixel coordinates, which is then tracked by downstream controllers. Controllers consume observations and a current waypoint and return a desired planar velocity that is mapped to (ω, θ) through the actuation calibration. At the evaluation level, the benchmark runner provides a unified logging and replay pathway. Each episode writes a single CSV row with standardized fields and can optionally record synchronized videos, which makes it straightforward to integrate MicroPush into external analysis pipelines and continuous evaluation workflows. As a practical path toward hardware integration, the same control interface can be used with real-time visual feedback, where observations are provided by a vision front end and commands

are sent to a magnetic actuation system, enabling sim-to-real validation with minimal changes to the algorithm stack.

C. Design goals

MicroPush is designed to satisfy four system-level goals relevant to reproducible algorithm development for contact-rich micromanipulation:

- 1) **Physics-grounded fidelity with lightweight computation.** The simulator captures the dominant effects in rolling microrobot pushing, including overdamped motion, stick-slip contact, near-field resistance, and optional background flow, while remaining efficient for rapid iteration and large-scale runs.
- 2) **Modularity across the autonomy stack.** Planning, control, and learning components interact through clean interfaces, allowing researchers to replace global planners, task-level planners, or controllers without altering simulator internals.
- 3) **Reproducible benchmarking and comparable metrics.** MicroPush provides deterministic seeding, standardized task suites (transport and assembly), unified logging, and consistent evaluation metrics to enable apples-to-apples comparison and controlled ablations.
- 4) **Research usability and extensibility.** The GUI accelerates debugging and demonstration, while the headless runner supports systematic evaluation; the same tasks

and dynamics are exposed through an RL interface to facilitate integration of learning-based approaches.

Together, these design choices make MicroPush a practical and reproducible testbed that supports contact-rich microrobot manipulation and enables fair, reproducible study and comparison of planning, control, and learning methods at the microscale under clutter and flow.

D. Simulator core

We implement a lightweight 2D interaction simulator for low-Reynolds-number micromanipulation with magnetically actuated rolling microrobots. The simulator is designed for contact-rich pushing and includes contact dynamics, near-field hydrodynamic resistance, and an optional background flow field. The world evolves in a planar workspace with a fixed time step Δt . All geometric quantities are maintained in simulator coordinates and are mapped to physical micrometers through a constant scale factor.

1) Physical model:

a) *Overdamped dynamics and actuation:* We model the microrobot and cells as rigid disks moving in a viscous-dominated regime. Let $\mathbf{p}_i \in \mathbb{R}^2$ denote the position of object i and let \mathbf{v}_i denote its translational velocity. Under the overdamped assumption, velocities are proportional to the net applied force:

$$\mathbf{v}_i = \mathbf{u}_i + \gamma_i^{-1} \mathbf{F}_i, \quad (1)$$

where γ_i is an effective drag coefficient and \mathbf{F}_i aggregates interaction terms such as contact response and wall penalties. For passive cells, $\mathbf{u}_i = \mathbf{0}$. For the microrobot, \mathbf{u}_r is determined by the actuation command, consisting of a rolling frequency ω (Hz) and a heading θ (rad).

We use an empirical calibration to map the driving frequency to the free-space rolling speed in the synchronous regime (Fig. 2). Specifically, we fit a through-origin line to measured speed–frequency data over $[0, \omega_{\max}]$ with $\omega_{\max} = 30$ Hz and obtain $k_v = 2.3 \mu\text{m/s/Hz}$:

$$v_0(\omega) = k_v \omega, \quad \mathbf{u}_r = v_0(\omega) \begin{bmatrix} \cos \theta \\ \sin \theta \end{bmatrix}. \quad (2)$$

At higher frequencies, the robot exhibits step-out and the speed deviates from the linear mapping. We therefore restrict actuation commands to $\omega \leq \omega_{\max}$. To model actuation variability, we apply bounded noise to the commanded speed magnitude and heading. State integration uses explicit Euler:

$$\mathbf{p}_i^{t+1} = \mathbf{p}_i^t + \mathbf{v}_i^t \Delta t. \quad (3)$$

b) *Wall boundary conditions:* We enforce a rectangular workspace using a penalty force when an object penetrates the boundary. For an object of radius r_i at $\mathbf{p}_i = (x_i, y_i)$ inside a domain of width W and height H , the wall force is

$$\mathbf{F}_i^{\text{wall}} = k_w \begin{bmatrix} \max(0, r_i - x_i) - \max(0, x_i - (W - r_i)) \\ \max(0, r_i - y_i) - \max(0, y_i - (H - r_i)) \end{bmatrix}, \quad (4)$$

where k_w is a wall stiffness coefficient.

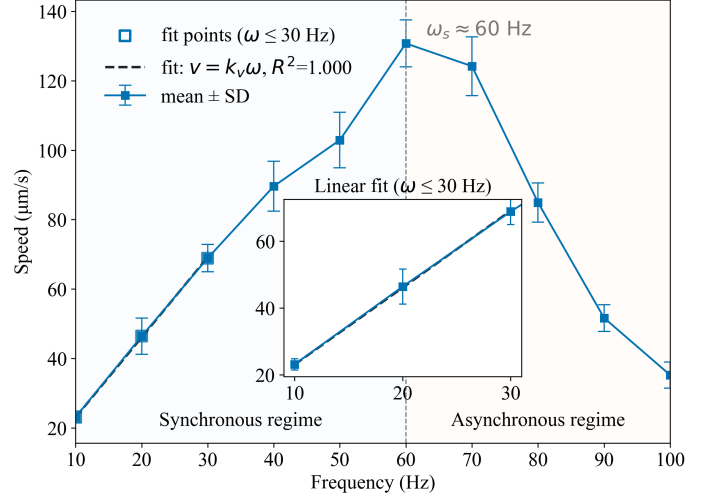


Fig. 2. Free-space rolling speed versus driving frequency. Markers show the mean speed and error bars indicate ± 1 SD across trials. A through-origin linear fit in the low-frequency synchronous range $\omega \leq 30$ Hz yields $k_v = 2.3 \mu\text{m/s/Hz}$ used in Eq. (2). The vertical dashed line indicates the frequency at which the measured speed reaches its maximum; beyond this point, the speed no longer follows the linear mapping due to step-out effects.

c) *Contact and stick–slip friction:* Each object is a disk with radius r_i . For a pair (i, j) , define the center distance $d_{ij} = \|\mathbf{p}_j - \mathbf{p}_i\|$ and the overlap

$$\delta_{ij} = (r_i + r_j) - d_{ij}. \quad (5)$$

When $\delta_{ij} > 0$, we apply a Hertz-type normal law

$$F_{ij}^n = k_h \delta_{ij}^{3/2}, \quad \mathbf{F}_{i \leftarrow j}^n = F_{ij}^n \mathbf{n}_{ij}, \quad (6)$$

where $\mathbf{n}_{ij} = (\mathbf{p}_j - \mathbf{p}_i)/d_{ij}$.

Fig. 3 summarizes the geometric quantities used in pairwise interactions. Let \mathbf{t}_{ij} be a unit tangent orthogonal to \mathbf{n}_{ij} and let $\mathbf{v}_{\text{rel}} = \mathbf{v}_i - \mathbf{v}_j$. We decompose $v_n = \mathbf{v}_{\text{rel}} \cdot \mathbf{n}_{ij}$ and $v_t = \mathbf{v}_{\text{rel}} \cdot \mathbf{t}_{ij}$. To emulate Coulomb friction in an overdamped setting, we implement friction at the velocity level by limiting the tangential relative motion per step. We define the maximum tangential correction budget as

$$v_{\max} = \mu F_{ij}^n (\gamma_i^{-1} + \gamma_j^{-1}) \Delta t. \quad (7)$$

If $|v_t| \leq v_{\max}$, we enforce sticking by canceling the tangential relative component. Otherwise, we apply slipping by reducing $|v_t|$ by v_{\max} . To improve numerical stability with finite Δt , we additionally cap the normal relative approach per step and apply a small velocity-level correction to avoid excessive interpenetration during contact-rich interactions.

d) *Near-field hydrodynamic damping:* We approximate near-field hydrodynamic resistance as a reduction in the separation rate when the gap $h_{ij} = d_{ij} - (r_i + r_j)$ is small but positive. When $0 < h_{ij} \leq h_{\text{th}}$ and $\dot{h}_{ij} > 0$ (the pair is separating), we reduce the separation rate:

$$\dot{h}_{ij}^{\text{target}} = (1 - \beta) \dot{h}_{ij}, \quad 0 < \beta < 1. \quad (8)$$

The threshold h_{th} increases mildly with separation speed and is capped:

$$h_{\text{th}} = \text{clip}(h_0 + \alpha \max(0, \dot{h}_{ij}), h_0, h_{\max}). \quad (9)$$

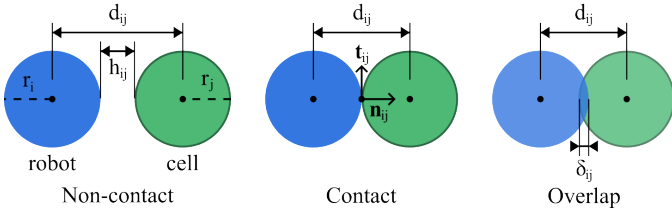


Fig. 3. Geometric quantities for a robot and cell pair used in contact handling and near-field hydrodynamic damping. The center distance is d_{ij} , the gap is $h_{ij} = d_{ij} - (r_i + r_j)$, and the overlap is $\delta_{ij} = (r_i + r_j) - d_{ij}$. The unit normal \mathbf{n}_{ij} points from object i to j , and the tangential direction \mathbf{t}_{ij} is orthogonal to \mathbf{n}_{ij} .

e) *Guard band for imminent contact*: To prevent numerical tunneling when two objects are close but not yet in contact, we clamp the closing motion when $0 < h_{ij} \leq g$ by setting the normal component of the relative velocity to zero. This yields stable contact onset without requiring extremely small Δt .

f) *Optional background Poiseuille flow*: When enabled, we superimpose a 2D Poiseuille profile along $+x$:

$$\mathbf{v}^{\text{flow}}(y) = \begin{bmatrix} U_{\max} (1 - \xi^2) \\ 0 \end{bmatrix}, \quad \xi = 2 \left(\frac{y}{H} \right) - 1. \quad (10)$$

We treat the flow as an additive drift velocity and add it to all objects after computing the interaction and boundary responses. See Movie S5 for cell pushing under Poiseuille flow.

g) *Overlap resolution*: After integration, we apply a position-level projection step to resolve small residual overlaps by separating penetrated pairs along \mathbf{n}_{ij} .

2) *Interface and observations*: The simulator provides a single-step API used by both the interactive GUI and the headless benchmark runner. At each step, the controller supplies an actuation command (ω, θ) , the engine advances the world by one simulation step, and an observation dictionary is returned. Observations include the robot pose and velocity, per-cell positions and velocities, and object radii. For convenience, the same quantities are available in both simulator coordinates and physical units.

For reproducibility, all stochastic components are controlled by a user-provided random seed. All physical and numerical parameters are stored in a centralized parameter set to support transparent tuning and controlled ablation studies.

E. Planning module

MicroPush computes a global, obstacle-avoiding reference path from the current simulator state. At each planning call, we rasterize the workspace into a binary occupancy mask $I \in \{0, 1\}^{H \times W}$, where H and W are the mask height and width in pixels. Occupied pixels represent obstacles and free pixels represent traversable space (Fig. 4). The start point is the center of the moving object, either the microrobot or a designated cell. The planner outputs a piecewise-linear polyline $\mathcal{Q} = \{q_\ell\}_{\ell=1}^N$ in the same pixel grid. To improve comparability across planners and robustness for downstream waypoint-following controllers, we resample \mathcal{Q} using a fixed

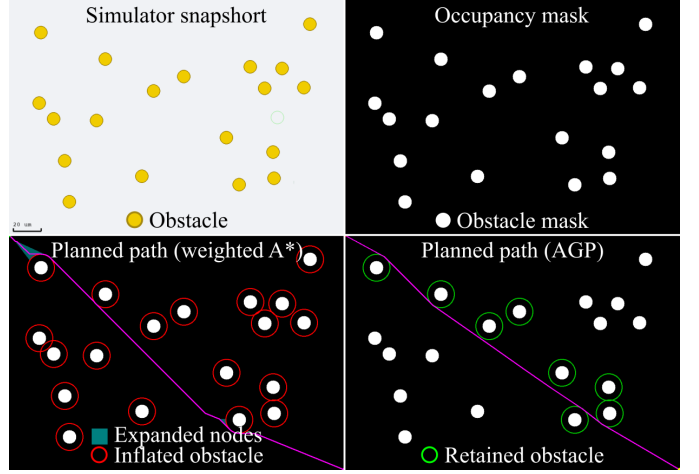


Fig. 4. Global planning in MicroPush. A simulator snapshot is rasterized into a binary occupancy mask. Both planners use the same obstacle inflation model in Eq. (11). The weighted A* baseline expands nodes on the inflated grid, whereas AGP operates in continuous geometry and prunes irrelevant obstacles before constructing waypoints.

arc-length spacing Δs (pixels) while preserving the first and last vertices.

To account for the size of the moving body, we plan in an inflated space by expanding each obstacle k to

$$R_k = r_k^{\text{obs}} + r_{\text{move}}, \quad (11)$$

where r_k^{obs} is the obstacle radius estimated from the minimum enclosing circle of its raster contour (pixels) and r_{move} is the pixel-space radius of the moving object. Both global planners described below consume the same inflation model in Eq. (11) and return a resampled polyline \mathcal{Q} to be tracked by the low-level controller.

1) *Global planning*: From the occupancy mask, we extract connected components of occupied pixels as obstacle instances. Since obstacles are circular in the planning layer, each contour is summarized by its minimum enclosing circle, yielding an estimated center c_k and radius r_k^{obs} (pixels). We then compute the inflated obstacle radius R_k using Eq. (11).

a) *Analytic Geometry Planner (AGP)*: We use the Analytic Geometry Planner (AGP) as the default global planner. AGP operates on the set of inflated obstacle circles in continuous 2D geometry and returns a collision-free, piecewise-linear reference path with low computational overhead. In brief, AGP proceeds in three stages. First, it prunes obstacles that are irrelevant to the straight-line start-to-goal corridor using a tunable corridor parameter α , retaining only circles whose inflated safety regions can interact with the ideal path. Second, it advances waypoints by constructing tangents to a small set of nearby inflated circles and selecting the next waypoint that maintains forward progress toward the goal. Third, it connects consecutive waypoints into a polyline, which is then resampled at a fixed spatial step for downstream waypoint tracking (Fig. 4). The geometric construction details are provided in [29]; here we integrate AGP into MicroPush through the shared inflation model in Eq. (11).

b) *Weighted A**: As a standard grid-based baseline, we implement Weighted A* on an 8-connected lattice defined over

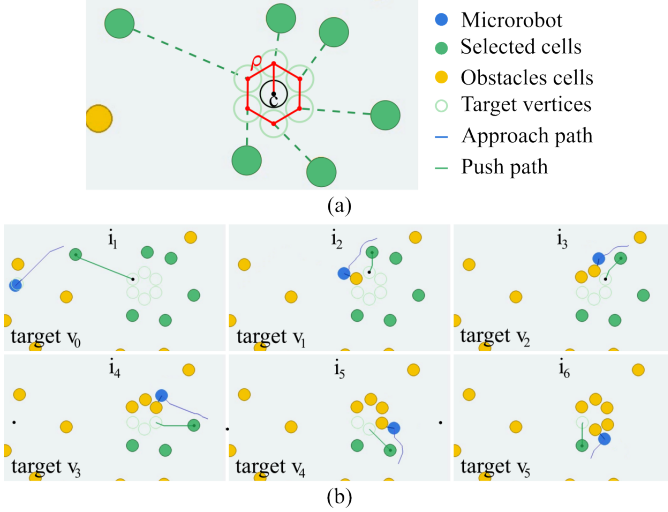


Fig. 5. Task-level planning for hexagonal assembly. (a) From hexagon center c and radius ρ , the planner defines target vertices $\{v_j\}_{j=0}^5$ and assigns six cells to vertices (dashed lines). (b) Example execution over the ordered sequence i_1, \dots, i_6 : the global planner generates an approach path (blue) to establish contact and a push path (green) to drive the selected cell toward its assigned target vertex; the approach ends at a pre-contact reference point for control.

free pixels of the inflated occupancy mask. Obstacle inflation follows Eq. (11). Weighted A* evaluates a node n by

$$f(n) = g(n) + w h(n), \quad (12)$$

where $g(n)$ is the accumulated path cost with unit cost for cardinal moves and $\sqrt{2}$ for diagonal moves, $h(n)$ is the Euclidean distance-to-goal heuristic, and $w > 1$ biases the search toward the goal to reduce planning time at the expense of optimality. The resulting grid path is converted to a screen-space polyline and resampled before being passed to the controller.

2) *Task-level planning*: While the global planner produces a collision-aware polyline to a specified goal, micromanipulation tasks often require deciding which object to move next and where to place it. MicroPush therefore includes a lightweight task-level planner that maps the current simulator state to a short sequence of subgoals for multi-object assembly (see Movie S4 for a representative hexagonal assembly execution).

a) *Hexagonal assembly objective*: We consider an assembly task that arranges cells on the vertices of a regular hexagon. Given a desired hexagon center $c \in \mathbb{R}^2$ (screen space) and a radius ρ (pixels), the target vertex set is

$$v_j = c + \rho \begin{bmatrix} \cos(\frac{2\pi}{K}j + \phi) \\ \sin(\frac{2\pi}{K}j + \phi) \end{bmatrix}, \quad j = 0, \dots, K-1, \quad (13)$$

with $K = 6$ and a fixed rotation $\phi = \pi/6$. For ρ , we use a biologically reasonable default proportional to the cell radius, e.g., $\rho \approx 2.6 r_{\text{cell}}$, which creates small inter-cell gaps that facilitate cell patterning. The target vertices and an example of cell-to-vertex assignment are shown in Fig. 5(a).

b) *Fast selection, assignment, and ordering*: Let B be the number of available cells and let $K = 6$ be the number of target vertices. The task-level planner produces a sequence $\{(\text{idx}_A^{(t)}, g^{(t)})\}_{t=1}^T$, where $\text{idx}_A^{(t)}$ is the selected cell index and

$g^{(t)} \in \{v_j\}$ is its assigned vertex. For efficiency, we use a heuristic pipeline with three components.

First, we perform selection and assignment using a Hungarian solve on the full $B \times K$ cost matrix $C_{ij} = \|p_i - v_j\|_2$. When $B \geq K$, the assignment yields K matched pairs, which simultaneously selects K cells and assigns each selected cell to a distinct vertex.

Second, we determine an execution order over the selected cell-vertex pairs using a greedy nearest-neighbor rule, initialized from a small set of start choices and refined with a few passes of 2-opt.

Third, we apply a light local search that swaps vertex assignments between two selected cells if it reduces a surrogate objective

$$J = \sum_{i=1}^K \|p_i - v_{\pi(i)}\|_2 + \left(\|s - p_{i_1}\|_2 + \sum_{t=1}^{K-1} \|v_{\pi(i_t)} - p_{i_{t+1}}\|_2 \right), \quad (14)$$

which combines the placement cost with a linking term that encourages a locally coherent execution order across successive subgoals. Here $\pi(i) \in \{0, \dots, K-1\}$ denotes the vertex index assigned to cell i , s is the robot start position, and i_1, \dots, i_K is the task execution order. If $B < K$, the planner degrades gracefully by assigning the available cells to the first B vertices using an angle-based ordering around c .

c) *Integration with global planning and replanning*:

The task-level output is a short list of subgoals in screen coordinates. During execution, each subgoal $(\text{idx}_A^{(t)}, g^{(t)})$ is passed to the global planner to compute a collision-aware reference polyline. The low-level controller then tracks this polyline while pushing the specified cell toward its assigned vertex, as illustrated by the approach and push trajectories in Fig. 5(b). After each placement, or upon failure, the simulator state is updated and the sequence can be recomputed to remain robust to disturbances and contact-induced rearrangements.

F. Control module

MicroPush executes global plans using a low-level controller that tracks a contact-aware reference point in the same 2D pixel workspace as the planner output. At each time step, the controller receives an observation containing the current robot state and the state of a selected cell, together with a desired cell waypoint $g \in \mathbb{R}^2$ in pixel coordinates (the next point on the resampled push polyline). Because the simulator dynamics are overdamped, the controller computes a desired planar translational velocity in pixel space and maps it to the actuation command (ω, θ) . Here θ is the heading and ω (Hz) determines the commanded free-space speed through the calibration in Eq. (2). Obstacle avoidance is handled by the global planner, so the controller focuses on robust plan execution under contact interactions and disturbances.

1) *Contact-aware reference point*: Directly tracking the cell waypoint g can induce oscillations during approach and excessive overlap during pushing. Instead, both controllers track a contact-aware reference point defined relative to the

selected cell. Let $p_r \in \mathbb{R}^2$ denote the robot center, $c \in \mathbb{R}^2$ the selected cell center, and define the nominal pushing direction

$$t = \frac{g - c}{\|g - c\|_2}. \quad (15)$$

a) *Pre-contact reference*: We define a pre-contact offset distance

$$d_{\text{pre}} = r_{\text{robot}} + r_{\text{cell}} + d_0, \quad (16)$$

where r_{robot} and r_{cell} are the robot and cell radii in pixels and d_0 is a small clearance. The pre-contact reference point is placed behind the cell along the negative pushing direction:

$$p_{\text{pre}} = c - d_{\text{pre}} t. \quad (17)$$

b) *Contact detection and pushing reference*: We detect contact using a distance threshold

$$\|c - p_r\|_2 \leq r_{\text{robot}} + r_{\text{cell}} + \delta, \quad (18)$$

where δ is a small tolerance in pixels. Once contact is detected, we switch to a closer pushing reference point that maintains forward progress while limiting compression:

$$p_{\text{push}} = c - d_{\text{keep}} t, \quad d_{\text{keep}} = r_{\text{robot}} + \beta r_{\text{cell}}, \quad \beta \in (0, 1). \quad (19)$$

c) *Reference switching and transition*: The final tracking reference is $p_{\text{ref}} = p_{\text{pre}}$ during approach and $p_{\text{ref}} = p_{\text{push}}$ during pushing. To avoid stalling at the contact onset, we use a short transition after contact detection. During this transition, the reference is interpolated from p_{pre} toward p_{push} once the robot heading is sufficiently aligned with the pushing direction. This staged reference construction is shared by both MPC and PID and stabilizes behavior in contact-rich scenes. Fig. 6 summarizes the reference construction and representative closed-loop behavior with and without background flow.

2) *Model Predictive Control (MPC)*: The MPC controller computes a short-horizon sequence of planar velocities $u_k \in \mathbb{R}^2$ using the kinematic model

$$x_{k+1} = x_k + \Delta t u_k, \quad (20)$$

where $x_k \in \mathbb{R}^2$ is the robot position and Δt is the simulator step. At each control step, we treat the contact-aware reference point p_{ref} as constant over the horizon and minimize

$$\min_{\{u_k\}_{k=0}^{N-1}} \sum_{k=0}^{N-1} \left(\|x_k - p_{\text{ref}}\|_Q^2 + \|u_k\|_R^2 \right) + \|x_N - p_{\text{ref}}\|_{Q_f}^2 + \|u_0 - u_{\text{prev}}\|_S^2, \quad (21)$$

where $\|z\|_Q^2 \triangleq z^\top Q z$ and $Q, Q_f, R, S \succeq 0$. Here u_{prev} is the previously applied command, and the last term penalizes abrupt command changes. The resulting problem is a convex quadratic program. We solve it at each step and apply the first action u_0 in a receding-horizon manner.

After solving, we apply limits to improve robustness and ensure consistent actuation across scenes:

$$\|u_0\|_2 \leq v_{\text{max}}, \quad \|u_0 - u_{\text{prev}}\|_2 \leq \Delta u_{\text{max}}. \quad (22)$$

We then map u_0 to (ω, θ) :

$$\theta = \text{atan2}(u_{0,y}, u_{0,x}), \quad \omega = \frac{\|u_0\|_2 s_{\mu\text{m}/\text{px}}}{k_v}, \quad (23)$$

where $s_{\mu\text{m}/\text{px}}$ is the pixel-to-micrometer scale and k_v is the calibrated speed-per-Hz coefficient in Eq. (2). When the commanded speed is near zero, we hold the previous heading to avoid angle discontinuities.

3) *PID controller*: As a lightweight baseline, we implement a PID controller that generates a planar velocity command from the position error to the same contact-aware reference point:

$$e(t) \triangleq p_{\text{ref}}(t) - x(t) \in \mathbb{R}^2, \quad (24)$$

where $x(t)$ is the robot position. The PID controller outputs

$$u(t) = K_p e(t) + K_i \int_0^t e(\tau) d\tau + K_d \dot{e}(t). \quad (25)$$

We include standard practical modifications for robustness. First, we apply integral anti-windup by clamping the accumulated integral term element-wise. Second, we use a low-pass filtered derivative:

$$\dot{e}_f(t) = (1 - \alpha_d) \dot{e}_f(t - \Delta t) + \alpha_d \dot{e}(t), \quad (26)$$

and substitute \dot{e}_f for \dot{e} in Eq. (25). Finally, we apply the same speed and rate limits used by MPC:

$$\|u(t)\|_2 \leq v_{\text{max}}, \quad \|u(t) - u(t - \Delta t)\|_2 \leq \Delta u_{\text{max}}. \quad (27)$$

The velocity command is mapped to (ω, θ) using the same calibration as MPC. When $\|u(t)\|_2$ is near zero, we hold the previous heading to avoid angle discontinuities.

4) *Implementation notes*: Both controllers optionally support a user-specified pushing direction in direction-control mode. If the desired direction changes abruptly, we temporarily revert to the pre-contact reference for a short duration before resuming pushing. This hysteresis improves stability under rapid direction changes.

III. BENCHMARK PROTOCOL AND EVALUATION

MicroPush provides a standardized benchmark protocol for reproducible comparison of planning and control methods in contact-rich micromanipulation. This section first specifies the benchmark protocol, including tasks, scenario generation, execution stages, success criteria, metrics, and logging. We then report evaluation results under fixed baseline configurations using the open-source headless runner, which executes identical protocols and evaluation code across all methods.

a) *Extending the benchmark suite*: Although this paper evaluates two canonical tasks, the benchmark protocol is task-agnostic and is intended to be extended. A new task is specified by (i) an initialization rule that samples the scene and defines the manipulated objects, (ii) a goal generator that produces one or more target configurations in screen space, and (iii) task-specific termination conditions and success criteria. The staged execution structure is reusable across tasks. In particular, the approach stage can be retained to standardize navigation-to-contact behavior across controllers, while the push stage can be swapped to evaluate different feedback policies under identical dynamics and disturbances. All tasks share the same logging schema and metric computation pipeline, so newly added tasks automatically produce comparable CSV outputs and can be analyzed with the same scripts used in this paper.

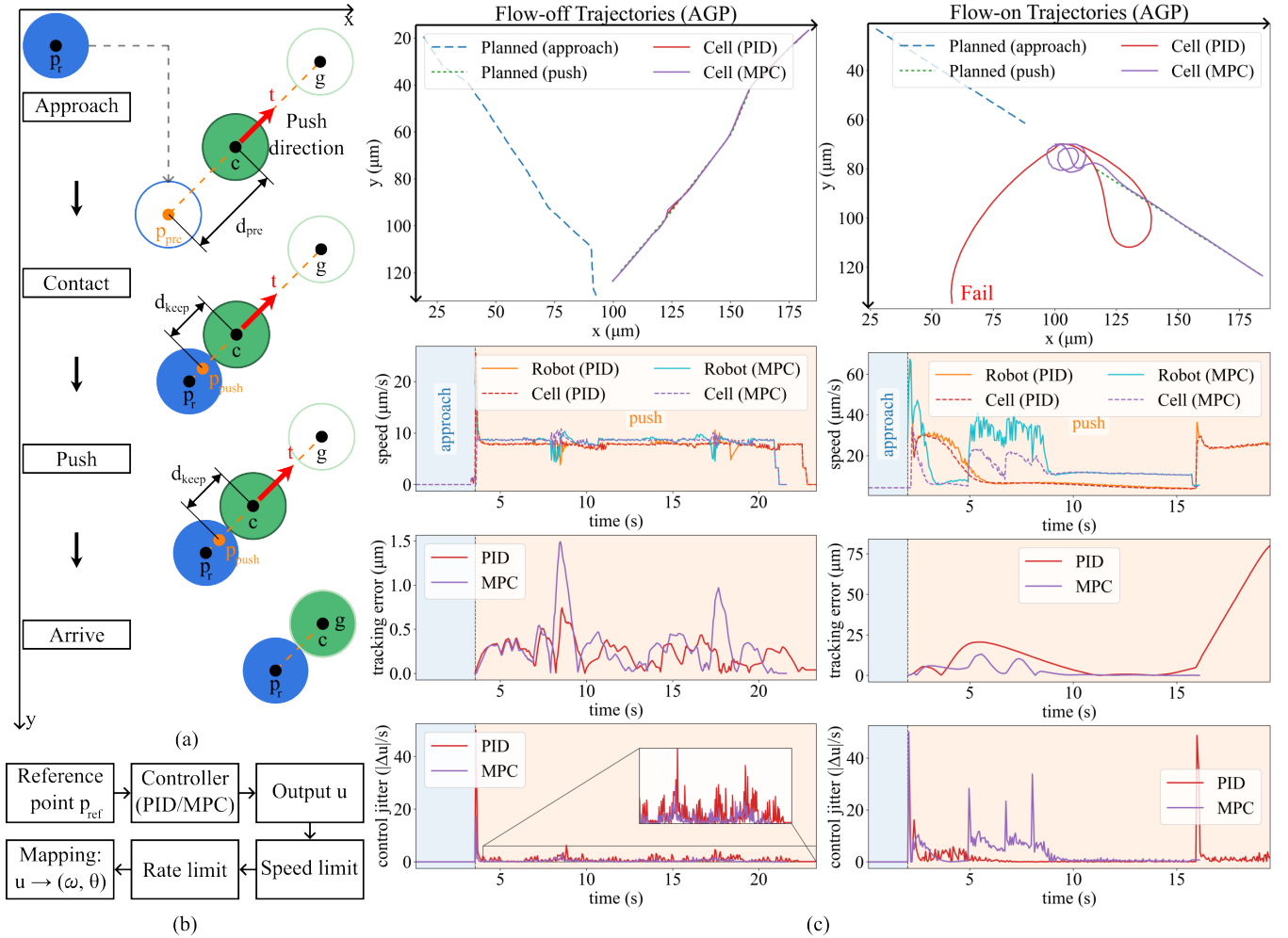


Fig. 6. Contact-aware reference point and representative controller behavior. (a) Reference construction for approach and pushing. The controller tracks a pre-contact point p_{pre} behind the cell to establish contact, then switches to a closer pushing point p_{push} to reduce compression while maintaining progress toward the cell waypoint g . (b) The controller outputs a planar velocity command, applies speed and rate limits, and maps it to the simulator actuation command (ω, θ) . (c) Representative trajectories and time series under AGP planning in flow-off and flow-on settings. Dashed curves show planned approach and push segments. Solid curves show resulting cell trajectories under PID and MPC. The speed, tracking error, and control jitter signals illustrate stability differences, and the flow-on case shows a representative PID failure (see Movie S7 for a qualitative MPC vs. PID comparison under flow).

A. Benchmark protocol

1) *Tasks and success definition*: We evaluate two tasks that capture complementary aspects of contact-rich pushing.

a) *T1: Single-object transport*: A selected cell is pushed to a fixed goal near the bottom-right of the workspace, while the microrobot starts near the top-left. This task evaluates approach, contact establishment, and sustained pushing. We report results under both flow-off and flow-on settings to separate clutter-induced deviations from flow-induced drift.

b) *T2: Multi-target assembly (hex pattern)*: Six cells are sequentially pushed to six target vertices forming a regular hexagon around a fixed workspace center. This task stresses long-horizon robustness under repeated contacts across multiple subtasks. We report overall success and execution-quality metrics defined in Section III-A4.

c) *Termination and success*: An episode terminates when either (i) the pushed cell center enters a success radius r_{succ} around the goal vertex, or (ii) the elapsed simulated time exceeds a timeout $T_{timeout}$. Unless otherwise stated, r_{succ}

follows the default used in the simulator GUI.

2) *Scenario generation and flow settings*: Each episode is initialized by a deterministic random seed that controls all simulator randomization, including scene initialization and actuation noise. We use disjoint seed sets across tasks and flow conditions. The released benchmark scripts provide the full command-line configuration and seed lists for exact replication.

a) *Defaults*: Benchmark defaults specify the workspace size, object radii, number of cells, actuation noise, flow strength, and timeout. Table I summarizes the default parameters used in this paper.

b) *Flow protocol*: For transport, we evaluate both flow-off and flow-on settings. For flow-on transport, we use a single pushed cell to isolate flow-induced drift from multi-cell interactions. For hex assembly, flow is disabled to avoid drift of already placed cells and to match the intended patterning protocol.

TABLE I
BENCHMARK DEFAULT PARAMETERS USED IN THIS PAPER. QUANTITIES
ARE IN PIXEL SPACE (PX) UNLESS NOTED.

Parameter	Value
Workspace size (W, H)	200×140 px (240×168 μm)
Robot radius r_{robot}	5.0 μm (4.17 px)
Cell radius r_{cell}	5.0 μm (4.17 px)
Cell number	20 (1 in transport with flow-on)
Time step Δt (s)	0.05
Actuation noise (speed/heading)	uniform ($\pm 2\%$ / ± 0.02 rad)
Flow strength U_{max} (flow-on)	5.0 $\mu\text{m/s}$ (centerline, Poiseuille)
Maximum running time T_{timeout} (s)	40

c) *Feasibility checks*: To avoid trivial infeasible initializations, we enforce simple geometric feasibility at initialization. For transport, the fixed goal must lie outside the inflated exclusion region of every cell in the initial scene. For hex assembly, the hexagon center and all target vertices must lie outside the inflated exclusion region of every cell in the initial scene.

d) *Time discretization*: All benchmarks use the simulator step size Δt . Given a timeout T_{timeout} , the maximum number of steps is

$$N_{\text{max}} = \left\lceil \frac{T_{\text{timeout}}}{\Delta t} \right\rceil. \quad (28)$$

3) *Execution protocol and controller interface*: Each episode follows a two-stage execution.

a) *Approach stage*: The global planner computes an approach polyline that moves the robot toward a pre-contact configuration relative to the selected cell. To reduce confounding from controller choices during navigation-to-contact, the approach stage uses the same waypoint-following policy for all baselines. The robot heading is set to the bearing toward the current approach waypoint, and the commanded frequency is

$$\omega = \text{clip}(k_d \|p_{\text{wp}} - p_r\|_2, 0, \omega_{\text{max}}), \quad (29)$$

with fixed parameters k_d and ω_{max} across all runs. The waypoint index advances when the robot is within a tolerance ϵ_{wp} of the current waypoint. The same tolerance is used to switch from approach to push after reaching the final waypoint.

b) *Push stage*: After approach completes, the system switches to pushing. The planner provides a push polyline for the selected cell. The evaluated controller (MPC or PID) receives observations and the current goal waypoint g in pixel coordinates and outputs an actuation command through the contact-aware reference construction in Section II-F1. To avoid near-zero command dead-zones in headless execution, we apply a small frequency floor during pushing when the cell remains outside the success radius. This rule is applied identically across all methods.

4) *Metrics*: We report the following metrics. All distances are converted to micrometers using the simulator scale.

a) *Success rate*: The fraction of episodes that terminate by success. We report Wilson 95% confidence intervals for binomial success rates where applicable.

b) *Time to success*: For successful episodes, the simulated time to reach the success region.

TABLE II
CSV LOGGING SCHEMA (ONE ROW PER EPISODE).

Field	Unit	Description
seed	–	deterministic episode seed
task	–	transport / assembly
planner	–	AGP / A*
controller	–	MPC / PID
flow_on	–	background flow enabled
status	–	success / timeout
sim_time_sec	s	simulated time to termination
steps	–	number of simulator steps
track_cell_mean_um	μm	mean push-path tracking error
cell_path_um	μm	pushed-cell path length
planned_push_um	μm	planned push polyline length
energy_df_sum	Hz	$\sum_t \omega_t - \omega_{t-1} $

c) *Push-path tracking error*: For successful episodes, the mean distance from the pushed cell center to the planned push polyline during the push stage. This is computed as the episode-level average of point-to-polyline distance evaluated at each push step.

d) *Pushed-cell path length and planned push length*: For transport, we report the arc-length of the pushed cell trajectory during the push stage and the length of the planned push polyline.

e) *Actuation variation*: Let ω_t denote the commanded actuation frequency at step t . We report

$$E_{\Delta\omega} = \sum_t |\omega_t - \omega_{t-1}|, \quad (30)$$

which serves as a proxy for command aggressiveness and jitter.

5) *Logging and reproducibility*: Each episode produces one CSV row. Table II summarizes the logged fields. The headless runner can optionally record synchronized videos for qualitative inspection.

a) *Reproducibility recipe*: MicroPush is deterministic given a random seed. After installing dependencies and cloning the repository, the main benchmark and the paired planner micro-benchmark can be reproduced with:

```
# (1) Full benchmark
# (transport + assembly; flow on/off)
python -m micro_push.run_benchmark \
  --task both --flow both \
  --seeds_transport 80 --seeds_hex 30 \
  --out bench_result.csv

# (2) Paired planner micro-benchmark
# (random static scenes)
python -m micro_push.run_planner \
  --seeds 100 --seed0 0 \
  --out micro_bench_result.csv
```

6) *Baselines and fixed hyperparameters*: We evaluate four planner and controller combinations for flow-off transport and hex assembly: AGP+MPC, AGP+PID, A*+MPC, and A*+PID. For flow-on transport, we focus on controller robustness and therefore report AGP+MPC and AGP+PID. Unless otherwise stated, all simulator, planner, and controller hyperparameters are fixed across runs. Table III lists the key hyperparameters.

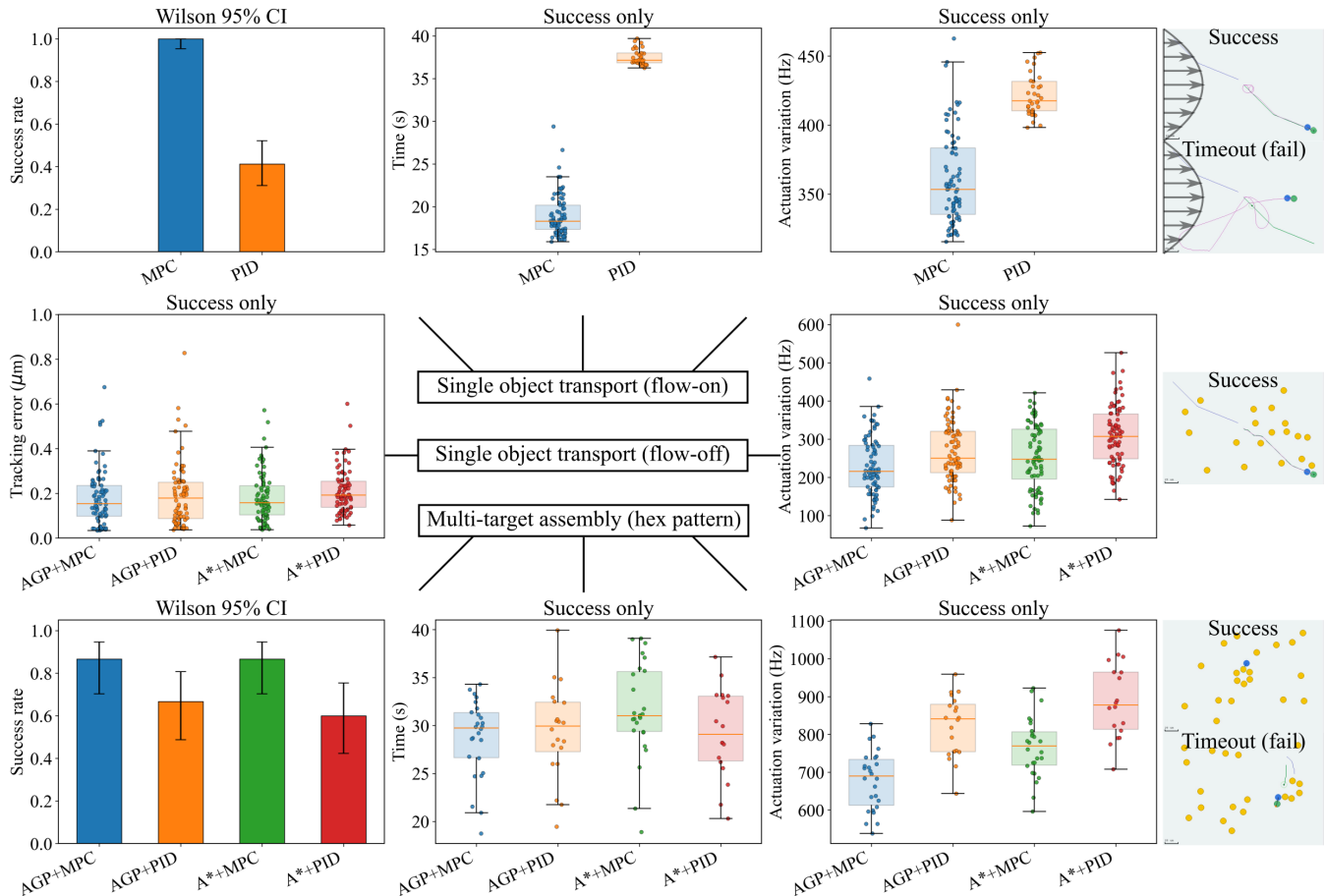


Fig. 7. Benchmark results for MicroPush. Top row: single-object transport with background flow enabled, comparing controller robustness using success rate with Wilson 95% confidence intervals, time to success, and the actuation-variation proxy $E_{\Delta\omega}$. Middle and bottom rows: flow-off benchmarks over four planner and controller combinations for transport and hex assembly. Boxplots and scatter overlays are computed over successful episodes only for continuous metrics. Insets on the right show representative trajectory snapshots from both successful and timed-out episodes under flow and clutter (see Movie S6).

TABLE III
KEY PLANNER/CONTROLLER HYPERPARAMETERS USED IN THIS PAPER
(FIXED ACROSS ALL RUNS UNLESS NOTED).

Parameter	Value
AGP corridor parameter α	3.0
A* heuristic weight w	1.1
MPC horizon N	10
MPC weights ($q_{\text{pos}}, r_{\text{ctl}}, s_{\text{smooth}}, qf_{\text{scale}}$)	(3.0, 0.12, 0.05, 6.0)
PID gains (K_p, K_i, K_d)	(4.0, 0.0, 0.8)
PID derivative LPF α_d	0.4
Max command frequency ω_{max}	30 Hz
Velocity rate limit (MPC/PID)	$0.8 v_{\text{max}}$ (px/s per step)
Pre-contact gap (MPC/PID)	0.8 (px)
Push-stage frequency floor	3.0 Hz
Success radius r_{succ} (px)	0.5

In this paper, we run $N_{\text{tr}} = 80$ episodes for transport under each flow condition and $N_{\text{hex}} = 30$ episodes for hex assembly under flow-off.

B. Evaluation results

1) *Closed-loop benchmark results:* Fig. 7 summarizes benchmark outcomes across tasks and flow conditions. Ta-

ble IV reports success rates over all runs and median values over successful runs for continuous metrics.

a) Flow-on transport stresses controller robustness:

Under background flow, disturbances continuously perturb contact and pushing direction. MPC achieves substantially higher success than PID (AGP+MPC: 1.000 vs. AGP+PID: 0.412) and reaches the goal faster when successful (median time 18.3 s vs. 37.1 s). PID also shows higher actuation variation (353 vs. 418), which is consistent with failures in which the pushed cell drifts away from the intended corridor.

b) Flow-off transport isolates execution quality under clutter:

With flow disabled, all combinations achieve high success rates under our protocol. Differences are primarily reflected in execution-quality metrics. MPC yields smaller tracking errors to the planned push polyline (AGP+MPC: 0.159 vs. AGP+PID: 0.189; A**+MPC: 0.158 vs. A**+PID: 0.193) and lower actuation variation than PID (AGP+MPC: 216 vs. AGP+PID: 250; A**+MPC: 248 vs. A**+PID: 307), indicating smoother velocity regulation during contact-rich pushing.

c) Hex assembly highlights long-horizon stability:

Hex assembly requires repeated contact acquisition and pushing across multiple subtasks, which reduces success relative to

TABLE IV

BENCHMARK SUMMARY. SUCCESS RATE IS COMPUTED OVER ALL RUNS. ALL OTHER METRICS ARE MEDIANS COMPUTED OVER SUCCESSFUL RUNS ONLY. WE REPORT THE ACTUATION VARIATION $E_{\Delta\omega} = \sum_t |\omega_t - \omega_{t-1}|$. FOR FLOW-ON TRANSPORT, WE REPORT AGP PLANNING ONLY TO FOCUS ON CONTROLLER ROBUSTNESS. FOR FLOW-OFF TRANSPORT, WE ONLY EVALUATE TRACKING ERROR.

Task	Flow	Baseline	N	Success	Time (s)	Track (μm)	CellPath (μm)	PlannedPush (μm)	$E_{\Delta\omega}$
transport	on	AGP+MPC	80	1.000	18.3	–	–	–	353
transport	on	AGP+PID	80	0.412	37.1	–	–	–	418
transport	off	AGP+MPC	80	0.988	–	0.159	144.2	135.8	216
transport	off	AGP+PID	80	1.000	–	0.189	140.0	135.7	250
transport	off	A*+MPC	80	1.000	–	0.158	136.9	137.4	248
transport	off	A*+PID	80	1.000	–	0.193	141.5	137.4	307
assembly	off	AGP+MPC	30	0.867	29.8	–	–	–	690
assembly	off	AGP+PID	30	0.667	30.0	–	–	–	841
assembly	off	A*+MPC	30	0.867	31.0	–	–	–	769
assembly	off	A*+PID	30	0.600	29.1	–	–	–	878

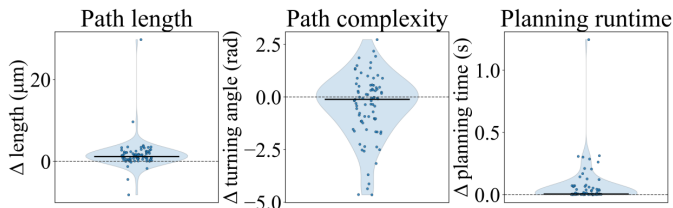


Fig. 8. Paired differences across random static scenes, computed as $\Delta = A^* - \text{AGP}$, for path length, turning angle, and planning runtime. Turning angle is computed as the sum of absolute heading changes along the resampled polyline.

single-object transport. MPC maintains higher success than PID for both planners (AGP+MPC: 0.867 vs. AGP+PID: 0.667; A*+MPC: 0.867 vs. A*+PID: 0.600). Across planners, PID also exhibits larger actuation variation (841 for AGP+PID and 878 for A*+PID) than MPC (690 for AGP+MPC and 769 for A*+MPC) and more frequent timeouts as contact-induced rearrangements accumulate.

d) *Qualitative failure modes*: The trajectory snapshots in Fig. 7 illustrate two common failure modes. Under flow, the pushed cell can drift away from the intended corridor, resulting in timeouts. In cluttered scenes, bystander contacts can divert the pushed cell from the planned push path and trigger repeated corrective maneuvers. These effects are amplified for PID due to larger command variation, whereas MPC more consistently stabilizes pushing by penalizing abrupt velocity changes.

2) *Paired micro-benchmark for global planners*: To isolate global planning behavior from contact dynamics and controller effects, we include a paired micro-benchmark in random static scenes. For each seed, both planners operate on the same inflated free space. We compute paired differences $\Delta = A^* - \text{AGP}$ for polyline path length, turning angle, and planning runtime (Fig. 8). Turning angle is computed as the sum of absolute heading changes along the resampled polyline. Table V reports summary statistics across paired scenes.

3) *Sensitivity to the success radius*: We additionally evaluate sensitivity to the success radius by tightening r_{succ} while keeping all other settings fixed. Table VI summarizes the resulting changes. Although absolute success rates decrease under stricter tolerances, the qualitative trends remain consis-

TABLE V

PAIRED MICRO-BENCHMARK OF THE TWO GLOBAL PLANNERS IN RANDOM STATIC SCENES. WE REPORT PAIRED DIFFERENCES $\Delta = A^* - \text{AGP}$ PER SEED. POSITIVE VALUES INDICATE SMALLER VALUES FOR AGP.

Metric	n	mean Δ	median Δ	$\text{Pr}(\Delta > 0)$
Path length (μm)	81	1.641	1.174	0.926
Turning angle (rad)	81	-0.456	-0.110	0.407
Planning time (s)	81	0.0604	0.00479	0.988

tent, with MPC outperforming PID under flow-on transport and maintaining stronger performance in hex assembly.

IV. CONCLUSION AND FUTURE WORK

We presented *MicroPush*, an open-source simulator and benchmark suite for contact-rich micromanipulation with magnetically actuated rolling microrobots. *MicroPush* couples an overdamped 2D interaction model with contact-aware stick-slip effects, lightweight near-field damping, and optional background flow, and exposes a modular planning-control stack with a practical two-phase manipulation strategy. To enable reproducible and fair comparison, we released a standardized benchmark protocol with deterministic seeds, staged execution, and unified metrics and CSV logging for large-scale evaluation on transport (with and without flow) and hexagonal assembly, complemented by a paired micro-benchmark that isolates global planning behavior. Across tasks, results indicate that feedback stability is the key driver of success under persistent flow disturbances and repeated contact events, while global planning can still affect execution smoothness through waypoint progression over long horizons.

There are several promising directions for future work. First, *MicroPush* can serve as a scalable training ground for reinforcement learning and imitation learning by leveraging the headless runner and standardized logging to collect data and benchmark learned policies against classical pipelines under identical protocols. Second, we plan to extend the benchmark to dynamic clutter by integrating online replanning and dynamic obstacle handling, enabling evaluation under time-varying scenes and moving cells. Third, we will close the loop with physical experiments by interfacing *MicroPush* with real microscope feedback and magnetic actuation hardware:

TABLE VI

SENSITIVITY TO THE SUCCESS RADIUS. WE TIGHTEN THE SUCCESS RADIUS FROM $r_{\text{succ}} = 0.5$ TO $r_{\text{succ}} = 0.2$ AND REPORT THE RESULTING CHANGES. Δ DENOTES $(r_{\text{succ}}=0.2) - (r_{\text{succ}}=0.5)$. SUCCESS IS COMPUTED OVER ALL RUNS; TIME IS THE MEDIAN OVER SUCCESSFUL RUNS ONLY.

Task	Flow	Baseline	Success			Time (s)		
			$r_{\text{succ}}=0.5$	$r_{\text{succ}}=0.2$	Δ	$r_{\text{succ}}=0.5$	$r_{\text{succ}}=0.2$	Δ
assembly	off	AGP+MPC	0.867	0.733	-0.134	29.8	30.8	0.9
assembly	off	AGP+PID	0.667	0.500	-0.167	30.0	29.2	-0.8
assembly	off	A*+MPC	0.867	0.533	-0.334	31.0	31.5	0.5
assembly	off	A*+PID	0.600	0.100	-0.500	29.1	33.7	4.6
transport	on	AGP+MPC	1.000	0.100	-0.900	18.3	31.1	12.9
transport	on	AGP+PID	0.412	0.013	-0.400	37.1	40.0	2.9
transport	off	AGP+MPC	0.988	0.988	-0.001	–	–	–
transport	off	AGP+PID	1.000	0.963	-0.038	–	–	–
transport	off	A*+MPC	1.000	0.975	-0.025	–	–	–
transport	off	A*+PID	1.000	0.925	-0.075	–	–	–

observations can be provided by a vision front end in the same state format, while the simulator actuation command (ω, θ) can be routed to hardware control, enabling systematic sim-to-real validation and model refinement using measured trajectories and contact events.

REFERENCES

- [1] Q. Wang, J. Zhang, J. Yu, J. Lang, Z. Lyu, Y. Chen, and L. Zhang, "Untethered small-scale machines for microrobotic manipulation: from individual and multiple to collective machines," *Acs Nano*, vol. 17, no. 14, pp. 13 081–13 109, 2023.
- [2] Z. Zhang, X. Wang, J. Liu, C. Dai, and Y. Sun, "Robotic micromanipulation: Fundamentals and applications," *Annual Review of Control, Robotics, and Autonomous Systems*, vol. 2, no. 1, pp. 181–203, 2019.
- [3] R. Xu and Q. Xu, "A survey of recent developments in magnetic microrobots for micro-/nano-manipulation," *Micromachines*, vol. 15, no. 4, p. 468, 2024.
- [4] K. T. Nguyen, G. Go, Z. Jin, B. A. Darmawan, A. Yoo, S. Kim, M. Nan, S. B. Lee, B. Kang, C.-S. Kim *et al.*, "A magnetically guided self-rolled microrobot for targeted drug delivery, real-time x-ray imaging, and microrobot retrieval," *Advanced Healthcare Materials*, vol. 10, no. 6, p. 2001681, 2021.
- [5] R. Pieters, H.-W. Tung, S. Charreyron, D. F. Sargent, and B. J. Nelson, "Rodbot: A rolling microrobot for micromanipulation," in *2015 IEEE International Conference on Robotics and Automation (ICRA)*. IEEE, 2015, pp. 4042–4047.
- [6] Y. Yang, F. C. Kirmizitas, M. Sokolich, A. Valencia, D. Rivas, M. Ç. Karakan, A. E. White, A. A. Malikopoulos, and S. Das, "Rolling helical microrobots for cell patterning," in *2023 International conference on manipulation, automation and robotics at small scales (MARSS)*. IEEE, 2023, pp. 1–6.
- [7] Y. Yang, D. Rivas, M. Sokolich, and S. Das, "Closed-loop control of bubble-propelled microrobots," in *2023 International Conference on Manipulation, Automation and Robotics at Small Scales (MARSS)*. IEEE, 2023, pp. 1–6.
- [8] Y. Yang, M. Sokolich, S. Mallick, and S. Das, "Quadrupole magnetic tweezers for precise cell transportation," *IEEE Transactions on Biomedical Engineering*, vol. 72, no. 4, pp. 1437–1444, 2024.
- [9] C. Pawashe, S. Floyd, E. Diller, and M. Sitti, "Two-dimensional autonomous microparticle manipulation strategies for magnetic microrobots in fluidic environments," *IEEE Transactions on Robotics*, vol. 28, no. 2, pp. 467–477, 2011.
- [10] M. Sokolich, C. Kirmizitas, S. Das, and R. Weiss, "Autonomous vision-based magnetic microrobotic pushing of micro-objects and cells," *arXiv preprint arXiv:2505.06450*, 2025.
- [11] Y. Jia, S. Miao, A. Wang, C. Ni, L. Feng, X. Wang, and X. Li, "Non-contact dexterous micromanipulation with multiple optoelectronic robots," *IEEE Robotics and Automation Letters*, 2025.
- [12] S. Mohanty, A. Paul, P. M. Matos, J. Zhang, J. Sikorski, and S. Misra, "Ceflowbot: A biomimetic flow-driven microrobot that navigates under magneto-acoustic fields," *Small*, vol. 18, no. 9, p. 2105829, 2022.
- [13] C. Dillinger, N. Nama, and D. Ahmed, "Ultrasound-activated ciliary bands for microrobotic systems inspired by starfish," *Nature communications*, vol. 12, no. 1, p. 6455, 2021.
- [14] R. Jitsho, N. Agharese, A. Okamura, and Z. Manchester, "A dynamics simulator for soft growing robots," in *2021 IEEE International Conference on Robotics and Automation (ICRA)*. IEEE, 2021, pp. 11 775–11 781.
- [15] W. Huang, X. Huang, C. Majidi, and M. K. Jawed, "Dynamic simulation of articulated soft robots," *Nature communications*, vol. 11, no. 1, p. 2233, 2020.
- [16] Z. Tan and D. Zhang, "Interactive ot gym: A reinforcement learning-based interactive optical tweezer (ot)-driven microrobotics simulation platform," in *2025 IEEE International Conference on Robotics and Automation (ICRA)*. IEEE, 2025, pp. 1–7.
- [17] N. Koenig and A. Howard, "Design and use paradigms for gazebo, an open-source multi-robot simulator," in *2004 IEEE/RSJ international conference on intelligent robots and systems (IROS)(IEEE Cat. No. 04CH37566)*, vol. 3. Ieee, 2004, pp. 2149–2154.
- [18] O. Michel, "Cyberbotics ltd. webots™: professional mobile robot simulation," *International Journal of Advanced Robotic Systems*, vol. 1, no. 1, p. 5, 2004.
- [19] E. Todorov, T. Erez, and Y. Tassa, "Mujoco: A physics engine for model-based control," in *2012 IEEE/RSJ international conference on intelligent robots and systems*. IEEE, 2012, pp. 5026–5033.
- [20] Y. Zhu, J. Wong, A. Mandlekar, R. Martín-Martín, A. Joshi, K. Lin, A. Maddukuri, S. Nasiriany, and Y. Zhu, "robosuite: A modular simulation framework and benchmark for robot learning," *arXiv preprint arXiv:2009.12293*, 2020.
- [21] L. Fan, Y. Zhu, J. Zhu, Z. Liu, O. Zeng, A. Gupta, J. Creus-Costa, S. Savarese, and L. Fei-Fei, "Surreal: Open-source reinforcement learning framework and robot manipulation benchmark," in *Conference on robot learning*. PMLR, 2018, pp. 767–782.
- [22] M. Ahn, H. Zhu, K. Hartikainen, H. Ponte, A. Gupta, S. Levine, and V. Kumar, "Robel: Robotics benchmarks for learning with low-cost robots," in *Conference on robot learning*. PMLR, 2020, pp. 1300–1313.
- [23] S. James, Z. Ma, D. R. Arrojo, and A. J. Davison, "Rlbench: The robot learning benchmark & learning environment," *IEEE Robotics and Automation Letters*, vol. 5, no. 2, pp. 3019–3026, 2020.
- [24] W. Amokrane, K. Belharet, M. Souissi, A. B. Grayeli, and A. Ferreira, "Macro-micromanipulation platform for inner ear drug delivery," *Robotics and Autonomous Systems*, vol. 107, pp. 10–19, 2018.
- [25] M. Tong, G. Huang, S. Zhuang, X. Yu, D. Hu, W. Lin, Y. Wu, Y. Chen, S. Cheng, M. Jiang *et al.*, "Robotic micromanipulation for patterned and complex organoid biofabrication," *Science Advances*, vol. 11, no. 36, p. eadz0808, 2025.
- [26] J.-P. Cieslik, X. Xia, and A. Salehi-Reyhani, "Magic-ot: an ai-guided optical tweezers platform for autonomous single-cell isolation in microfluidic devices," *Lab on a Chip*, 2026.
- [27] B. Calli, A. Walsman, A. Singh, S. Srinivasa, P. Abbeel, and A. M. Dollar, "Benchmarking in manipulation research: Using the yale-cmu-berkeley object and model set," *IEEE Robotics & Automation Magazine*, vol. 22, no. 3, pp. 36–52, 2015.
- [28] J. Luo, C. Xu, F. Liu, L. Tan, Z. Lin, J. Wu, P. Abbeel, and S. Levine, "Fmb: a functional manipulation benchmark for generalizable robotic

- learning,” *The International Journal of Robotics Research*, vol. 44, no. 4, pp. 592–606, 2025.
- [29] Y. Yang, M. Sokolich, F. C. Kirmizitas, S. Das, and A. A. Malikopoulos, “Microrobot vascular parkour: Analytic geometry-based path planning with real-time dynamic obstacle avoidance,” *arXiv preprint arXiv:2509.05500*, 2025.